Proceedings of ASME Turbo Expo 2011
GT2011
June 6-10, 2011, Vancouver, British Columbia, Canada

GT2011-46511

APPLICATION OF ENDWALL CONTOURING TO TRANSONIC TURBINE CASCADES: EXPERIMENTAL MEASUREMENTS AT DESIGN CONDITIONS

F. Taremi* and S.A. Sjolander†
Department of Mechanical and Aerospace Engineering
Carleton University, Ottawa, Ontario, Canada
ftaremi@connect.carleton.ca
ssjoland@mae.carleton.ca

T.J. Praisner‡
United Technologies, Pratt & Whitney
East Hartford, Connecticut, USA
thomas.praisner@pw.utc.com

ABSTRACT

An experimental investigation of the endwall flows in two transonic linear turbine cascades was presented at the 2010 ASME Turbo Expo (GT2010-22760). Endwall contouring was subsequently implemented in these cascades to control the secondary flows, and reduce the total pressure losses. The current paper presents experimental results from these cascades to assess the effectiveness of endwall contouring in the transonic flow regime. The experimental results include blade loadings, total pressure losses, streamwise vorticity and secondary kinetic energy distributions. In addition, surface flow visualization results are presented in order to interpret the endwall limiting streamlines within the blade passages.

The flat-endwall and contoured-endwall cascades produce very similar midspan loading distributions and profile losses, but exhibit different secondary flows. The endwall surface flow visualization results indicate weaker interaction between the secondary flows and the blade suction surface boundary layers in the contoured cascades. Overall, the implementation of endwall contouring results in smaller and less intense vortical structures, and the reduction of the associated secondary kinetic energy (SKE) and exit flow angle variations. However, the mass-averaged losses at the main measurement plane, located 40% axial chord lengths downstream of the cascade ($1.4C_X$), do not corroborate the numerically predicted improvements for the contoured cascades. This is in part attributed to slower mixing rates of the secondary flows in the compressible flow regime. The mass-averaged results at $2.0C_X$, on the other hand, show smaller losses for the contoured cascades associated with smaller SKE dissipation downstream of the cascades. Accordingly, the mixed-out row losses also show improvements for the contoured cascades.

INTRODUCTION

Gas turbine efficiency is strongly influenced by the entropy generation across the various turbomachinery components in the engine. Within the turbine stages, particularly in low aspect ratio blades, secondary losses due to endwall flows constitute as much as a third of the total entropy generation [1]. Consequently, in the past decade researchers have investigated methods for reducing the secondary losses in turbines, with much focus on non-axisymmetric endwall contouring. The majority of these investigations have been conducted in low-speed linear cascade facilities, which neglect the compressibility effects, and rotating test rigs with some inherent limitations on the spatial resolution of the experiments. The computational investigations, on the other hand, typically yield highly-resolved, trend-wise accurate results pertaining to the main flow features, but suffer from deficiencies associated with transition and turbulence modeling, leading to inaccurate loss predictions. This especially presents a problem with regard to the selection of an appropriate objective function for design studies such as endwall contouring or 3D blade stacking. The current study is aimed to improve the understanding of the secondary loss generating mechanisms in compressible flows using steady-state probe measurements from two transonic turbine cascades both with flat and contoured endwalls. The results from the contoured cascades are compared and contrasted with those from the baseline (flat) cascades, previously published by Taremi et al. [2]. The full-passage, non-axisymmetric endwall contouring design of Praisner et al. [3] was employed for the present configurations.

Secondary flow research in turbines, associated with the turning and separation of the endwall boundary layers, has received considerable attention in the past [4,5]. The main secondary flow structures are typically identified as the passage vortex, the counter vortex and the corner vortex. The passage vortex develops as an extension of the pressure-side leg of the horseshoe vortex, with its

---

* Ph.D. Student (Aerospace Engineering)
† Chancellor's Professor and Pratt & Whitney Canada Research Fellow
‡ Turbine Aerodynamics

growth and size largely influenced by the cross-passage pressure gradients [6-8]. The origin of the counter vortex, on the other hand, has been associated with different vortices such as the suction-side leg of the horseshoe vortex, the wall vortex induced by the passage vortex, and/or the trailing-shed vortex. These counter vortices form a semi-coherent structure downstream of the cascade, as they interact and coalesce, which is typically located above the passage vortex with an opposite sense of rotation. Closer to the endwall, the corner vortex appears in the interaction region between the pressure-side leg of the horseshoe vortex and the airfoil suction-surface boundary layer. The intensification of the corner vortex is mainly influenced by the transverse and streamwise pressure gradients in the aft part of the passage. Owing to the importance of intra-passage pressure gradients on secondary flow development, endwall contouring is utilized to modify the near-wall pressure distribution, and thereby to reduce the secondary losses.

Some of the earlier endwall contouring investigations looked at the effects of axisymmetric profiles in the presence of adverse [9] and favourable [10] streamwise pressure gradients. These studies showed significant reductions in total pressure loss and exit flow angle variations as a result of smaller and less intense passage vortices. The main design objectives were subsequently identified as: reducing the cross-passage pressure gradient in the forward part of the passage, decreasing the suction-side diffusion at the endwall following the airfoil suction peak, and minimizing the adverse streamwise pressure gradients due to contouring near the trailing edge. Over the past decade, the research groups at Rolls-Royce plc and Durham University [11-16] have designed and tested several non-axisymmetric profiled endwalls with the aim of minimizing the secondary kinetic energy (SKE) of the vortical structures and reducing the exit flow under/overturning. In most cases, the CFD predictions and the experimental results showed significant loss reductions for the contoured cascades. It was also confirmed that the loss reductions were not appreciably influenced by the transition behaviour on the endwalls [14]. Further investigations in a cold-flow rotating test rig substantiated the improvements due to endwall contouring downstream of the blade rows [17,18]. In one case, however, Ingram et al.'s experimental results [15] revealed large endwall separation, not predicted by CFD, for an "aggressive" contouring design, which ultimately led to higher losses albeit with smaller SKE. Other studies in low-speed linear cascades [19,20] and model test rigs [21,22] have also demonstrated the effectiveness of endwall contouring in both low- and high-pressure turbines.

More recently, Knezevici et al. presented low-speed experimental results from an aft-loaded cascade [23] and a front-loaded cascade [24] with different Zweifel coefficients. The measured improvements in loss, which exceeded the numerical predictions, were mainly attributed to the diminished size and strength of the passage vortex, reducing the associated freestream flow convection rates. This was also accompanied with smaller SKE and flow underturning, subsequently recognized as additional benefit in terms of the mixed-out losses.

In the current study, the experiments were performed in a transonic wind tunnel to account for the effects of flow compressibility. In what follows, the computational design of the contoured endwalls is first summarized, but the main focus is on the physical interpretation of the flow fields based on surface flow visualization results and pressure probe measurements. The results from the ongoing numerical studies will be presented in the future.

TURBINE CASCADES

Transonic Turbine Airfoils

The turbine airfoils in this study, referred to as SL1 and SL2, have the same inlet and outlet design flow angles, with a design row velocity ratio of approximately 2.6, but different aerodynamic loading levels: SL2 has a Zweifel coefficient that is 30% higher than that for SL1. The design inlet and outlet Mach numbers are 0.3 and 0.8, with a corresponding outlet Reynolds number of approximately 600,000. The relevant geometric and aerodynamic parameters of the cascades are summarized in Table 1. The axial velocity density ratio (at midspan) is defined as:

$$AVDR = \frac{\int_0^1 \left(\rho_2 u_2\right)_{MS} d\left(y/s\right)}{\int_0^1 \left(\rho_1 u_1\right)_{MS} d\left(y/s\right)} \tag{1}$$

The compressible form of the Zweifel coefficient is used to characterize the overall blade loading level at midspan:

$$Zw = \frac{s}{C_X} \frac{\gamma M_2^2 \cos\beta_2}{\left(1+\frac{\gamma-1}{2}M_{2,is}^2\right)^{\frac{\gamma}{\gamma-1}}-1} \left[\sin\beta_2 + \frac{1}{RVR}\sin\beta_1\right] \tag{2}$$

Table 1. SUMMARY OF CASCADE PARAMETERS

	SL1F	SL2F
Axial Chord, C_X (mm)	25.4	25.4
Blade Pitch, s (mm)	26.8	34.0
Blade Span, h (mm)	61.0	61.0
True Chord, C (mm)	31.0	33.7
Stagger Angle, ς (°)	34.9	41.2
Inlet Flow Angle, β_1 (°)	43.5	43.5
Outlet Flow Angle, β_2 (°)	69.0	68.2
Total Flow Turning, θ (°)	112.5	111.7
Axial Velocity Density Ratio, $AVDR$	0.98	1.02
Normalized Zweifel Coefficient, Zw/Zw_{SL1F}	**1.0**	1.3

In each case, two linear cascade configurations were examined: SL1F and SL2F with flat endwalls, and SL1C and SL2C with contoured endwalls. The experimental results from the flat-endwall cascades have been previously presented by Taremi et al. [2]. The blade surface flow visualization results showed evidence of small flow separations on the suction sides of both airfoils. In spite of the loading differences, both airfoils generated similar profile losses, possibly as a result of the separation bubbles. SL2F, on the other hand, exhibited stronger secondary flow structures and larger exit flow angle variations, resulting from the higher cross-passage pressure differences and the larger blade spacing. Consequently, SL2F produced higher secondary losses than SL1F, in part due to the mixing out and dissipation of the larger SKE downstream of the cascade.

Non-Axisymmetric Endwall Contouring

Several researchers have presented design methods for endwall contouring in the past [3,11,22,25]. The profiled endwall may be axisymmetric or non-axisymmetric, extending beyond or restricted to within the blade passage, and combined with three-dimensional blades and leading/trailing edge fillets. For the present study, the non-axisymmetric contoured endwalls were designed using a gradient-based optimization algorithm, coupled with compressible CFD simulations ($M_2 = 0.8$) with the following constraints:

- confined to the blade passage, referred to as "full-passage" contouring: 25 control points (5 pitchwise x 5 streamwise) with one degree-of-freedom in the wall-normal direction
- conserved flow capacity: matching the flat-endwall cases for midspan loading distributions, *AVDR* and exit flow angles
- applicable to existing blade rows: no blade modifications

An in-house (PWA) 3D RANS code, second-order accurate in space and time, was used to compute the flow fields. The simulations were performed using the *k-ω* turbulence model and the transition model described by Praisner and Clark [26] (applied only to the airfoils). In each case, the computational domain extended from the endwall to midspan with approximately 800,000 nodes per passage ($y^+ \approx 1$). The endwall contouring design was carried out using optimization software with the goal of minimizing the mass-averaged row losses. As many as 1000 design iterations were performed to arrive at the final optimized contoured geometries. Additional simulations were performed to investigate the effects of the transition model, inlet free-stream turbulence and inlet boundary layer thickness (based on wind tunnel measurements) on the predicted row losses. The computational results showed very similar benefits for the contoured cascades in all cases, albeit with small differences in the predicted loss coefficients. In particular, the simulation results with the transition model indicated approximately 10% lower losses in both flat and contoured cascades compared to the fully turbulent simulations.

The contoured endwalls shown in Figure 1 display several distinct geometric features, the most prominent of which is the cross-passage ridge "R" in SL2C. In SL1C, the ridge is located closer and almost parallel to the pressure surface in the aft part of the passage. Figure 1 also displays depressions or troughs "T" and protrusion or humps "H", which locally modify the static pressure distributions. These features are also identified in the surface flow visualization pictures for clarity. The endwall spanwise displacement due to contouring varies from about -5% to +20% C_X. As a potential adverse effect, the application of contouring increases the endwall surface areas compared to the flat-endwall cascades: 16% increase in SL1C and 10% increase in SL2C.

In Figure 1, convex endwall curvature acts to locally accelerate the flow, and thereby reduce the static pressure near the pressure surface (H). Concave endwall curvature, on the other hand, raises the local static pressure. The resulting changes in the endwall pressure distribution are expected to retard the development of the passage vortex, and delay its interaction with the suction-surface boundary layer. Additional improvements may result from a diminished counter vortex (smaller contribution from the wall-vortex induced by the passage vortex), leading to smaller losses and smaller SKE. The cross-passage ridge in the aft part of the passage is also intended to alter the trajectory of the passage vortex. The amplitude and location of the ridge stem from the optimization procedure, giving rise to differences between SL1C and SL2C designs. By the trailing edge plane the displacement due to contouring returns to the nominal endwall height (i.e. contouring restricted to the passage), producing regions of adverse and favourable streamwise pressure gradients across the pitch. The effects of contouring on the endwall limiting streamlines will be discussed with reference to the flow visualization pictures.

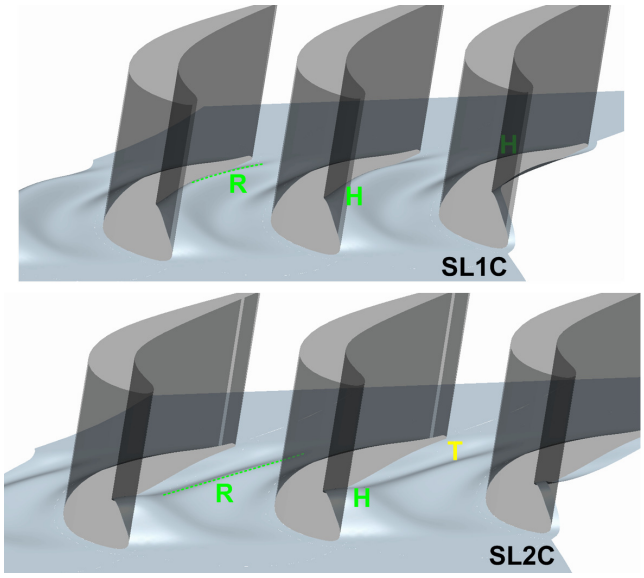

Figure 1. ENDWALL CONTOURING FEATURES

The pitch-averaged total pressure loss predictions for all four cascades, normalized using the midspan losses for SL1F, are presented in Figure 2a. As shown, the contoured endwalls do not affect the losses at midspan. The extents of the profile flow regions, on the other hand, have increased with the application of contouring due to smaller secondary flow penetration depths. The secondary losses associated with the counter and passage vortices have decreased significantly, although with a small increase in peak pitch-averaged loss values. The CFD predictions indicate plane-averaged loss reductions of 3% for SL1C and 7% for SL2C.

The pitch-averaged exit flow angles in Figure 2b display smaller flow under/overturning for the contoured cascades. The locations of maximum underturning have shifted closer to midspan, particularly in SL2C, due to reduced passage vortex intensity (greater counter vortex influence). Even though the application of contouring has not increased the overturning at 5% span, the position of maximum overturning has moved closer to the endwall in SL2C. Approaching the endwalls, the corner vortices decrease the overturning below 5% span, resulting in additional near-wall losses as shown in Figure 2a. In this region SL1C shows some benefit, whereas SL2C does not. Although not shown here, the contoured cascades also display weaker vortical structures and produce smaller SKE. Overall, the numerical predictions in Figure 2 are in agreement with the low-speed findings, presented in [3]. The aim of the current experimental study is to quantify the effects on mass-averaged and mixed-out losses in high-speed flows.

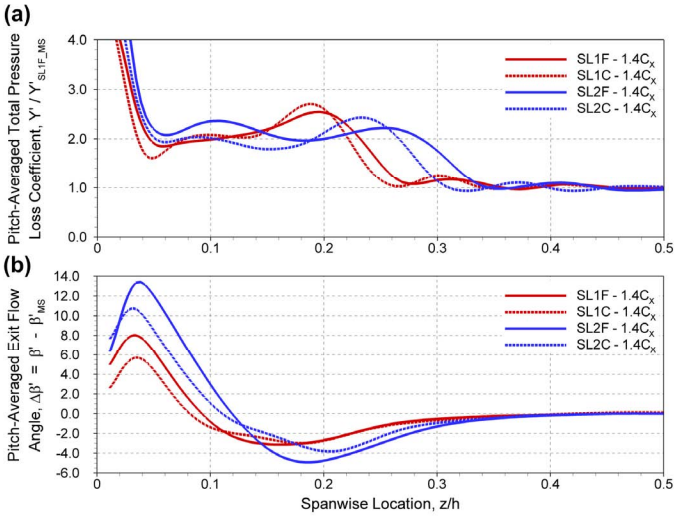

Figure 2. CFD PREDICTIONS: (a) NORMALIZED PITCH-AVERAGED TOTAL PRESSURE LOSS COEFFICIENTS AND (b) FLOW ANGLES

EXPERIMENTAL APPARATUS AND PROCEDURES

Test Section and Instrumentation

The experimental investigations were conducted in the Pratt & Whitney Canada High-Speed Wind Tunnel laboratory at Carleton University. The wind tunnel, shown schematically in Figure 3, is of the blow-down type with typical run durations of approximately 40 seconds. In this facility, the Mach number at the outlet of the turbine cascade can be varied from about 0.3 to 1.4.

The inlet freestream total pressure is recorded for every data point using a Pitot Probe and used to normalize all other pressure measurements. The inlet total temperature is also collected at every data point to determine the air density at the outlet of the cascade, assuming adiabatic expansion. A turbulence generating grid is installed about 60 axial chord lengths upstream of the cascade and normal to the flow direction. The resultant inlet freestream turbulence intensity and length scale are approximately 4% and $0.6C_X$, respectively. The inlet endwall boundary layers were traversed using a Pitot probe (D = 0.9 mm), and the results are presented in Table 2. The application of endwall contouring in the cascades did not affect the inlet boundary layers. Moreover, net secondary losses (generated inside the blade row) have been found to be insensitive to inlet boundary layer thickness in the past [5].

Within the blade passages, blade-surface static pressure taps were used to investigate the midspan loading distributions, and these are presented in the Results section. A seven-hole pressure probe (D = 1.8 mm) was used to document the downstream flow fields according to the probe calibration and data reduction procedures in [27]. The effects of flow quality on pressure probe measurements in this wind tunnel have been investigated in detail, and are described in [28]. The inlet static pressure taps, shown in Figure 4, were used to confirm inlet flow pitchwise uniformity (i.e. no pitchwise variation in inlet static pressure). Outlet flow blade-to-blade periodicity was investigated by traversing the midspan wakes over the middle five passages. Furthermore, the axial velocity density ratio was measured to be very close to 1.0, which is indicative of acceptable two-dimensionality of the profile flow.

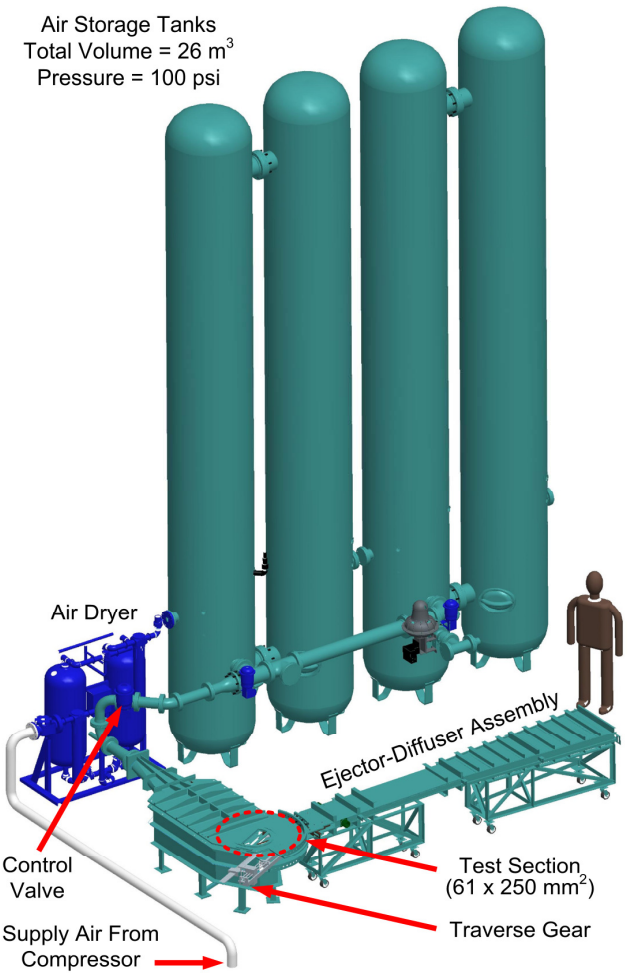

Figure 3. PRATT & WHITNEY CANADA HIGH-SPEED WIND TUNNEL

Table 2. INLET ENDWALL BOUNDARY LAYER PARAMETERS

	$M_{1,MS}$	$M_{2,is}$	$\delta_{99\%}$ (mm)	$\delta_{99\%}/h$	δ^* (mm)	δ^*/h	θ (mm)	θ/h	H	Re_{δ^*}	Re_θ
SL1F	0.286	0.78	17	0.28	1.94	0.032	1.40	0.023	1.4	17,000	12,200
SL2F	0.283	0.78	17	0.28	1.95	0.032	1.39	0.023	1.4	17,500	12,400

The outlet isentropic Mach number and the midspan blade loading distributions, as predicted by CFD, were used to set the wind tunnel operating point for all subsequent measurements.

As shown in Figure 4, the main measurement plane was located at 140% axial chord lengths downstream of the leading-edge ($1.4C_X$). Additional probe measurements were collected at $2.0C_X$. A step-motor-driven traverse gear was used to traverse the three-dimensional flow field downstream of the middle blade passage. The measurement grid is superimposed on the contour plot in Figure 4, where SS and PS indicate suction and pressure sides of the wake, respectively. Seven-hole probe measurements were collected at 15 spanwise positions (41 pitchwise data points / position). The closest traverse to the endwall was limited to 3% span to avoid wall interference effects on probe measurements [29].

The data acquisition system employed three absolute and eight differential *Druck* pressure transducers. At each data point 200 samples were collected at a sampling rate of 2 kHz, and the

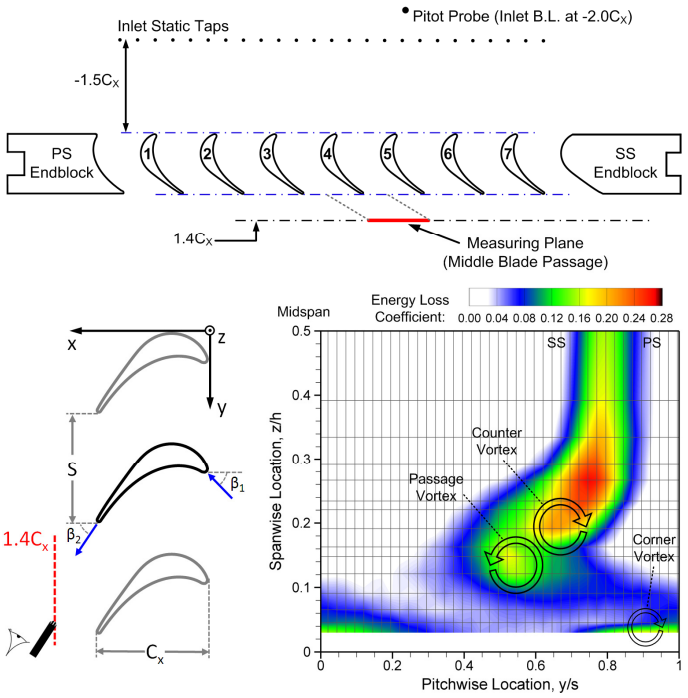

Figure 4. TURBINE CASCADE FLOW FEATURES

samples were arithmetically averaged. The selections of the sampling rates and times have been described in [30].

Data Reduction and Experimental Uncertainties

Several definitions for the energy loss coefficient (ζ) have been presented in the past [31]. Here, the energy loss coefficient was defined as:

$$\zeta = \frac{T_0\left(s_2 - s_1\right)}{h_0 - h_{2,is}} \cong \frac{\left(\frac{\gamma-1}{\gamma}\right)\ln\left(\frac{P''_{01}}{P''_{02}}\right)}{1-\left(1+\frac{\gamma-1}{2}M^2_{2,is}\right)^{-1}} \qquad (3)$$

where the double primes indicate overall mass-averaged. The definition of the energy loss coefficient was slightly modified for the contour plots: the inlet freestream total pressure ($P_{01,MS}$) and the downstream local total pressures (P_{02}) were used instead of the mass-averaged values in Equation 3, and the results were weighted by the local mass flux (ζ x $AVDR$).

Several additional parameters were investigated to compare the strengths of the secondary flow fields downstream of the cascades. The secondary flow parameters were derived from the velocity components normal to the primary flow direction shown in Figure 4 (β_2):

$$\beta'_{MS} = \tan^{-1}\left(\frac{v'_{MS}}{u'_{MS}}\right) \quad \text{and} \quad \Delta\beta' = \beta' - \beta'_{MS} \qquad (4)$$

The components of the vorticity vector were estimated using the Crocco relation, as outlined by Perdichizzi [32]:

$$\omega_X = \frac{\partial w}{\partial y} - \frac{\partial v}{\partial z} \quad \text{and} \quad \omega_Y = \frac{1}{u}\left(v\omega_X + \frac{a^2}{\gamma}\frac{\partial \ln P_0}{\partial z}\right) \qquad (5)$$

and the streamwise vorticity coefficient was defined as:

$$C\omega_S = \frac{C}{U_{2,is}}\left(\omega_X \cos\beta'_{MS} + \omega_Y \sin\beta'_{MS}\right) \qquad (6)$$

where $U_{2,is} = M_{2,is}\sqrt{\gamma RT}$

The secondary velocity components and the secondary kinetic energy coefficient were obtained using:

$$v_{sec} = v\cos\beta'_{MS} - u\sin\beta'_{MS} \quad \text{and} \quad w_{sec} = w \qquad (7)$$

$$C_{SKE} = \frac{\rho\left(v^2_{sec} + w^2_{sec}\right)}{\gamma P_{2,MS} M^2_{2,is}} \qquad (8)$$

Further details regarding the data reduction and the averaging procedures, and the treatment of the near-wall results (0 to 3% span) can be found in [29].

Some of the key factors influencing the uncertainties in this experiment were described in [33]; these included the effects of shear flow, turbulence and Reynolds number on multi-hole pressure probe measurements, in addition to the relatively small errors associated with probe calibration, data acquisition and data reduction procedures. Additional measurements were collected using a Kiel probe (total pressure) for comparisons with the 7-hole probe results, and these were found to be in very close agreement.

The experimental uncertainty analysis was initially performed using the method of Moffat [34]. The uncertainties were also investigated by means of repeatability studies to account for any other sources of error, which may have been neglected by the Moffat approach (local turbulence, shear flow, etc.). Consequently, the values shown in Table 3 represent the most conservative (i.e. largest) estimates of uncertainties in this experiment.

Table 3. EXPERIMENTAL UNCERTAINTIES

Flow Angles, α and β	± 1°
Mach Number, M	± 0.01
Static Pressure, P	± 2% $P_{dynamic}$
Total Pressure, P_0	± 1% $P_{dynamic}$
Integrated SKE Coefficient, C''_{SKE}	± 0.0005

RESULTS AND DISCUSSION

Midspan Blade Loading Distributions

The midspan surface Mach number distributions are presented in Figure 5, which also illustrates the close agreement between the CFD results and the experimental measurements. The loading distributions are presented in terms of the normalized surface length (S/S_{max}) to show the diffusion experienced by the blade-surface boundary layers.

As evident from Figure 5, SL2 is more highly loaded than SL1. Since the two airfoils (different geometries) have the same inlet and outlet flow angles and Mach number ratio, the 30% increase in Zweifel coefficient has been achieved with larger blade spacing in SL2, as indicated in Table 1. The additional loading for SL2 results in larger cross-passage pressure differences in the forward part of the passage. This is typically found to enhance the growth of the passage vortex, as will be seen in the streamwise

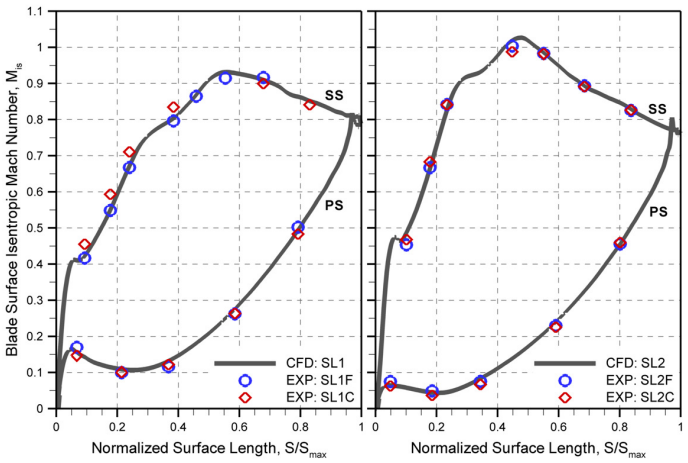

Figure 5. AIRFOIL ISENTROPIC MACH NUMBER DISTRIBUTIONS

vorticity plots. Adverse pressure gradients are evident on the aft part of the airfoils, past the suction peaks. The suction-surface boundary layer characteristics are also affected by the loading distributions. The results in Figure 5 suggest earlier transition on SL2 (sonic flow at 0.5 S/S_{max}) than on SL1, which is more aft-loaded. Additional details regarding the loading distributions and the profile losses may be found in [2].

Flow Visualization Results

The surface flow visualization studies were conducted using a fluorescent-dye/oil mixture, illuminated and photographed under ultra-violet lighting (following the completion of the tests), and the results are presented in Figure 6. The nomenclature of Sieverding [4] was used to interpret the limiting streamlines: dashed lines are used for flow separation, dotted lines for flow reattachment and arrows for surface shear stress vectors. Also marked are the locations of the protrusions and the depressions on the contoured endwalls, while the approximate positions of the ridges are shown with green dashed lines. Other regions of raised static pressure, as compared to the flat endwalls, are identified with ⊕. The surface flow visualization results for the flat-endwall cascades have been presented in [2], and therefore the focus in this paper is on the differences due to endwall contouring.

In Figure 6, A_1 marks the saddle point of inlet boundary layer separation, and S_1 is the resulting primary separation line. In the contoured cascades, the position of A_1 has shifted in both pitchwise and axial directions due to changes in endwall static pressure distributions. In Figures 6b and 6d, the inlet boundary layer streams approaching the blade passages experience local acceleration (H) or diffusion as compared to the flat endwalls, induced by pitchwise variations in the channel heights. The resulting streamline curvature displaces A_1 in the pitchwise direction towards the centre of the passage. A_1 and S_{1S} are also shifted upstream, indicating slightly earlier inlet boundary layer separation, which is particularly noticeable in the more highly-loaded SL2C cascade. These results, congruent to the findings in [23], indicate changes in horseshoe vortex formation and inlet boundary layer entrainment due to contouring [20].

Moving downstream, S_2 marks the liftoff line of the horseshoe vortex and the start of the new endwall boundary layer. In both contoured cases, the distance between A_1 and S_2 has increased relative to the flat endwalls. The main difference between SL1C and SL2C is revealed in the formations of the pressure-side legs, S_{1P} and S_{2P}, and this is attributed to the high static pressure regions on the endwalls stemming from the automated optimization procedure (solutions with minimum row losses). In SL1C, the region of raised static pressure extends upstream of S_{2P} and through the blade passage at approximately 70% pitch. Consequently, the distance between S_{1P} and S_{2P} has increased when compared to Figure 6a. On the other hand, in SL2C the ⊕ region is both smaller and more localized. Furthermore, the SL2 loadings (Figure 5) display stronger cross-passage pressure differences in the forward part of the passage with significantly lower suction-surface static pressures, which ultimately result in smaller flow convergence between S_{1P} and S_{2P} in Figure 6d. Overall, endwall contouring leads to weaker interaction [4] between S_{2P} and the suction-surface boundary layers in both cases. This is typically found to reduce the size of the passage vortex and the resulting losses [24], which will be discussed further in the next sections.

The new endwall boundary layer that forms downstream of S_2 is swept across the passage by the transverse pressure gradients. An important objective of contouring is to reduce the strength of this crossflow within the passage. As shown in Figures 6b and 6d, the shear stress vectors in the contoured cascades are more closely aligned with the nominal streamwise directions up to about $0.8C_X$. In SL2C, this is primarily attributed to the hump and the cross-passage ridge, which alter the trajectory of the passage vortex. Subsequently, in each case the passage vortex may undergo fewer revolutions (also suggested by the downstream helicity distributions, not shown here), which is anticipated to reduce the entrainment of the low-momentum endwall-boundary-layer fluid. In Figure 6d, the large surface shear stresses near the hump also suggest closer proximity of the passage vortex to the endwall. Downstream of S_{2P} and along the suction surface ($0.7C_X$ in Figure 6b), the second protrusion is expected to alleviate the adverse streamwise pressure gradients in the aft part the passage (Figure 5), that would otherwise enhance the passage vortex both in size and in radial migration.

Figures 6b and 6d also display differences in the location and extent of the ridge and the trough. In SL1C, the ridge as an extension of the hump reduces the static pressure in the pressure side of the passage, thereby alleviating the transverse pressure difference acting on the passage vortex. In SL2C, the cross-passage ridge, originating at the hump and extending towards the suction surface, accelerates the endwall crossflow in the nominal streamwise direction. The differences due to contouring are especially evident from the mid-passage shear stress vectors in Figures 6c and 6d. In the aft-part of the passage in Figure 6d, the surface streamlines over the trough are turned towards the suction surface under the influence of raised static pressure. This is also evident close to the trailing-edge plane, possibly leading to corner vortex intensification, as the wall displacement due to contouring returns to its initial (pre-passage) height. Subsequently, another high shear stress line (black dashed line) is identified downstream of the trough in Figure 6d, which will be further clarified with reference to the streamwise vorticity plots. Downstream of the

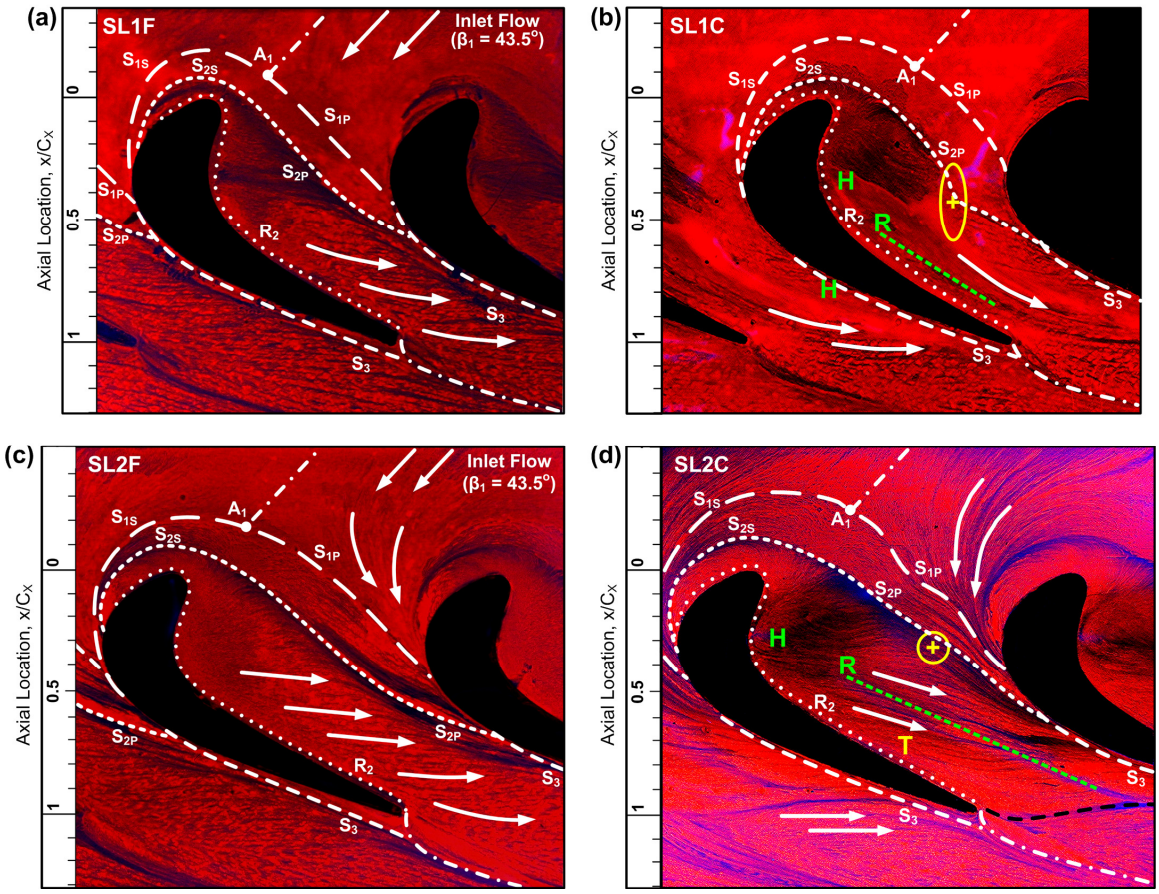

Figure 6. ENDWALL SURFACE FLOW VISUALIZATION RESULTS ($M_{2,IS} \approx 0.8$): (a) SL1F, (b) SL1C, (c) SL2F AND (d) SL2C

cascades, the corner vortices are displaced away from the suction surfaces, possibly due to trailing edge separation near the endwalls.

Downstream Flow Field Measurements at $1.4C_X$

Presentation of the downstream flow field measurements includes the following parameters obtained from the seven-hole probe: energy loss coefficient, streamwise vorticity coefficient, exit flow angles and secondary kinetic energy coefficient. The results are presented in both contour plot format and pitch-averaged plots. The overall-integrated values are summarized at the end.

Figure 7a shows colour floods of streamwise vorticity coefficient ($C\omega_S$), superimposed with contour lines of mass-weighted energy loss coefficient (ζ x $AVDR$). The results are plotted over one blade pitch ($0 < y/s < 1$) and half span ($0 < z/h < 0.5$) with appropriate pitch-to-chord ratios (Table 1). The higher loading in SL2 is associated with the larger blade spacing, which is evident from Figure 7a (larger pitch-to-span ratio). The local variations in mass flux have been incorporated in these plots for consistency with the final mass-averaged results (see [29] for additional discussion). Based on the right-handed Cartesian coordinate system shown in Figure 4, the passage vortex has positive vorticity, and the counter and corner vortices have negative vorticity. The pitch-averaged flow angles, depicting the classic under/overturning characteristic, are shown in Figure 7b.

SL1F and SL1C results show similar losses and secondary flow structures: the sizes and locations of the vortical structures and the secondary loss penetration depths have not been significantly altered by contouring. However, contouring has slightly decreased the intensities of the passage vortex and the counter vortex. Consequently, the pitch-averaged exit flow angles show approximately 1° reduction in underturning. SL1C also shows a small decrease in secondary losses, as will be discussed in the next sections. Even though the differences are not significant, the results support the CFD predictions regarding the reductions in loss and flow underturning. Furthermore, contouring has not increased the overturning near the endwall at around 5% span. These results comprise the baseline case for the contouring design, in which the new endwall features shown in Figure 1, and the resultant increased wetted area (+16%) have not adversely affected the performance of this moderately aft-loaded transonic cascade.

In general, the more highly loaded SL2 cascade displays stronger secondary flow structures than SL1. Application of endwall contouring has greatly reduced the sizes and strengths of the passage and counter vortices. SL2C displays only one distinct loss core, as opposed to the two loss cores in SL2F, with a slightly lower magnitude (ζ x $AVDR$ = 0.24). The locations of the vortical structures and the pitchwise extent of the secondary losses, on the other hand, have not been significantly affected by contouring. The loss core associated with the counter vortex in SL2C has migrated slightly closer to midspan, perhaps indicative of larger spanwise static pressure gradients. The intensity of the corner vortex, which

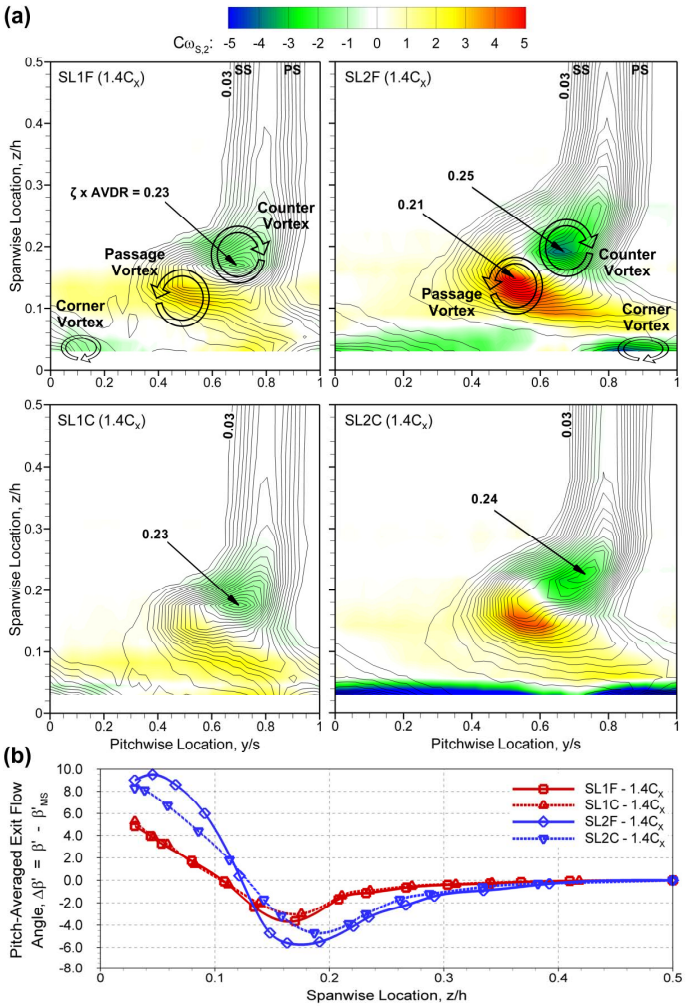

Figure 7. (a) STREAMWISE VORTICITY COEFFICIENTS ($C\omega_S$) AND (b) PITCH-AVERAGED EXIT FLOW ANGLES AT 1.4C$_X$

stretches almost entirely across the pitch in SL2C, has increased. This intensification is mainly attributed to the trough in Figure 1 as discussed with reference to the trailing-edge shear stress line in Figure 6d. The pitch-averaged exit flow angles are in reasonable agreement with the CFD predictions in Figure 2b. Contouring has resulted in approximately 2° reduction in both underturning, with a small shift towards midspan, and overturning below 10% span. The more uniform exit flow angle distribution, sometimes used as the objective function for contouring design [11], would reduce losses due to off-design incidence in any subsequent blade rows. The reduced under/overturning also affects the spanwise variations in mass flux, and consequently the mass-weighted loss contours in Figure 7a; regions of underturning and overturning are associated with high and low mass fluxes, respectively [29]. Accordingly, SL2C displays higher mass-weighted loss coefficients than SL2F from 5% to 10% span. In summary, the application of contouring has resulted in weaker secondary flow structures without significantly altering the losses at 1.4C$_X$. This suggests that the design-oriented CFD simulations, indicating 7% plane-averaged loss reduction in SL2C, overpredict the loss generation due to mixing within the blade rows. Additional simulations, with up to ten million nodes, are currently under way to examine the effects of various turbulence models on the predicted row loss generation.

Another important parameter related to the production of secondary loss is the secondary kinetic energy associated with the vortical structures. Figure 8a shows colour floods of secondary kinetic energy coefficient (C_{SKE}), overlaid with secondary velocity vectors ($\overline{V_{sec}} + \overline{W_{sec}}$). Also shown are the pitch-averaged C_{SKE} in Figure 8b. C_{SKE} is predominantly a function of the secondary velocities, and to a lesser extent of the local variations in density (Equation 8). Large values of C_{SKE} are found in the interaction regions between the passage vortex and the counter vortex. The largest secondary velocities, found in SL2F at around 15% span, are up to 20% of the value of the primary velocity (U_2). Closer to the endwall, large pitchwise secondary velocities are induced by the action of the passage vortex (flow overturning).

The application of contouring has resulted in slightly smaller secondary velocities and C_{SKE} in SL1C. This is particularly evident for the passage and counter vortices as anticipated from Figure 7a. The smaller SKE at 1.4C$_X$ may also reduce the mixing losses downstream, which will be discussed in the next sections. Consistent with the findings in Figure 7a, the contouring features in SL1C (baseline loaded case) do not bring about any deleterious effects. The SL2C results in Figure 8a show significant improvements compared to SL2F: up to 30% reduction in the magnitude of the secondary velocities and 50% reduction in peak values of C_{SKE} between 10% and 25% span. In this region, the secondary velocities display similar spanwise and pitchwise components since the relative locations of the vortices have not shifted noticeably. The secondary velocities also indicate that freestream fluid is continuously convected into the secondary loss core, shown by the red arrows in Figure 7a, thereby producing additional shearing losses downstream. Closer to the endwall (below 5% span), both SL2F and SL2C show large pitchwise secondary velocities induced by the passage vortex. The effects of the counter-rotating corner vortex on the secondary velocities in this region, although small, can be seen between 0 and 20% pitch in SL2C. Finally, the pitch-averaged results in Figure 8b confirm the qualitative assessment of the contour plots; contouring greatly reduces the secondary kinetic energy, mainly associated with a diminished passage vortex.

Downstream Flow Field Measurements at 2.0C$_X$

Additional measurements were collected downstream of the cascades to document the progression of the secondary flows and determine the mixing losses. Figure 9a shows colour floods of C_{SKE} at 2.0C$_X$. Comparing these results to those in Figure 8a indicates significant diffusion and mixing of flow fields downstream of the cascades. The maximum loss values have decreased in all four cases, and the secondary losses occupy larger regions of the flow fields. Furthermore, there are marked reductions in the magnitudes of both secondary velocities and C_{SKE}.

SL1C produces slightly smaller loss cores and smaller C_{SKE} than SL1F, particularly below 10% span as shown in Figure 9b. On the other hand, they both display similar C_{SKE} at around 15% span, indicative of different mixing rates downstream of 1.4C$_X$. The mixing is more pronounced downstream of the SL2 cascades:

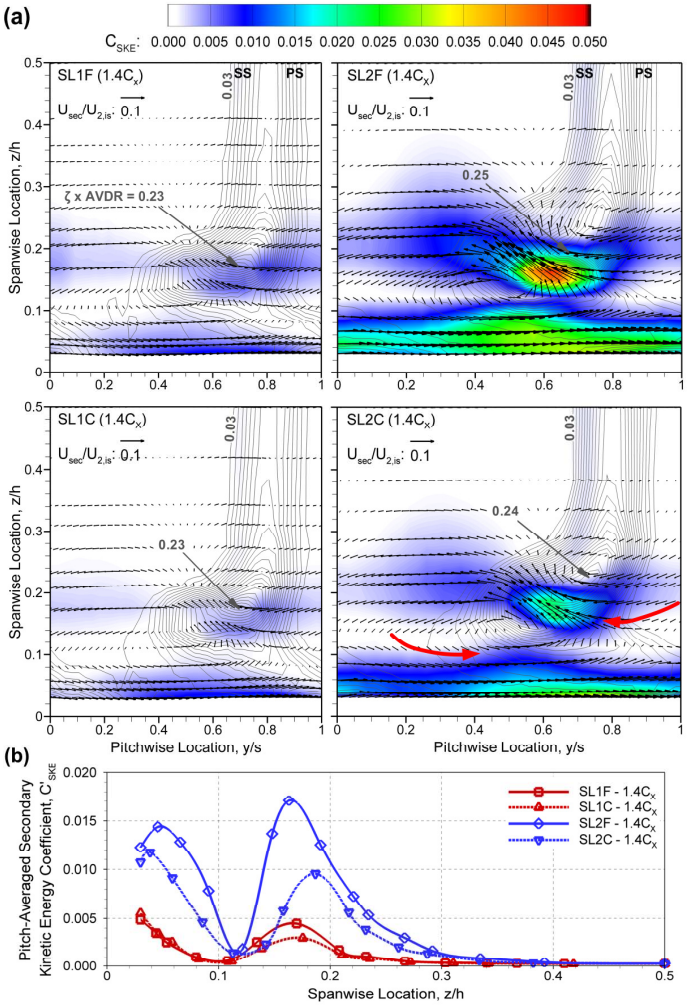

Figure 8. (a) C_{SKE} AND SECONDARY VELOCITIES AND (b) PITCH-AVERAGED C_{SKE} AT 1.4C_X

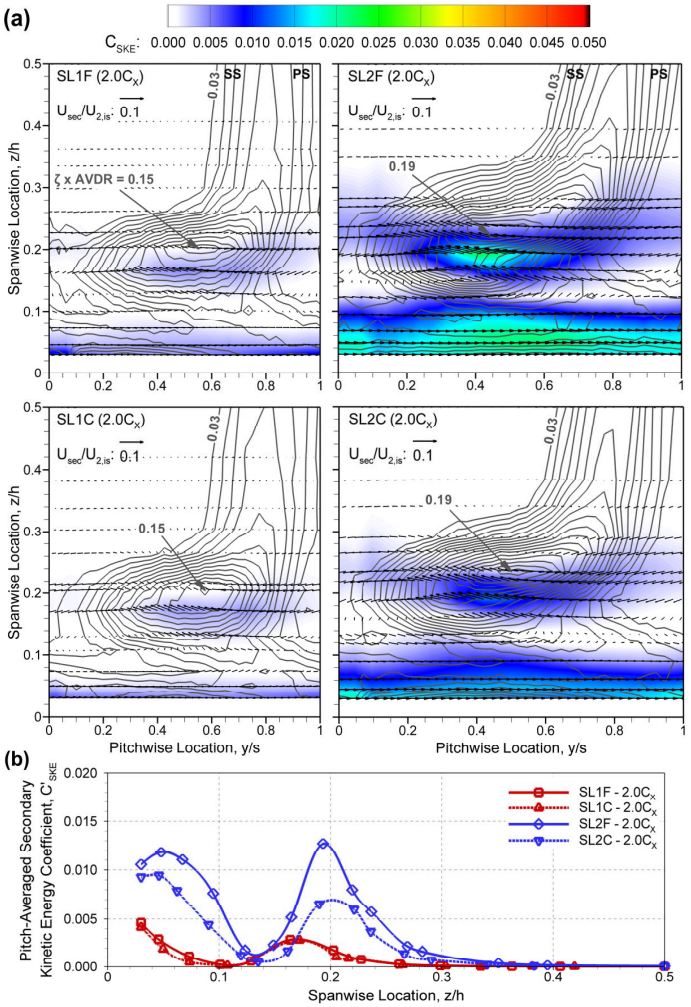

Figure 9. (a) C_{SKE} AND SECONDARY VELOCITIES AND (b) PITCH-AVERAGED C_{SKE} AT 2.0C_X

the two loss cores in SL2F (Figure 8a) have amalgamated into one, the secondary loss penetration depths have increased significantly, and the near-wall losses are mainly associated with the skewed endwall boundary layers below 5% span. The mixing-out and dissipation of the primary and secondary kinetic energy raises the losses in both cascades, and by 2.0C_X SL2C shows smaller losses than SL2F. These results stem from the differences in the intensities of the vortical structures (Figure 7a) and the associated C_{SKE} (Figure 8a) at 1.4C_X. In Figure 9a, the secondary velocities from 10% to 25% span have smaller spanwise components than those in Figure 8a, suggesting greater spanwise mixing rates (than pitchwise) between the two planes. The secondary velocities below 10% span, having primarily pitchwise components, are also significantly smaller due to weaker crossflows at the endwalls. Figure 9b also depicts the spanwise migration of the secondary flows with peak C_{SKE} values displaced towards midspan. Overall, the application of contouring in SL2 has positively influenced the flow field in terms of loss and C_{SKE} reductions. Moreover, the apparent flow non-uniformities at 2.0C_X indicate additional mixing losses yet to come, which will be discussed next.

Pitch-Averaged and Overall-Integrated Results

The pitch-averaged energy loss coefficients, normalized by the profile losses for SL1F at 1.4C_X, are shown in Figure 10a. As anticipated from the contour plots, SL1C shows slightly smaller losses than SL1F associated with less intense passage and counter vortices. The secondary losses increase downstream of the cascades, and the contributions of the near-wall losses, below 10% span, become more appreciable due to reduced overturning (larger mass fluxes). At 2.0C_X, SL1C displays higher losses than SL1F from 3% to 7% span due to larger SKE dissipation, between Figures 8a and 9a, in this region. The SL2 cascades also produce similar row losses at 1.4C_X, although small differences are apparent across the span. By 2.0C_X, SL2C displays smaller losses than SL2F in two distinct areas: 12% to 18% span (passage vortex) and 28% to 35% span (counter vortex). The SL2 results, however, show very similar losses from 3% to 10% span: contouring has not increased the near-wall losses. The spanwise loss distributions at 2.0C_X support the CFD predictions at 1.4C_X (Figure 2a) although still showing smaller improvements than predicted.

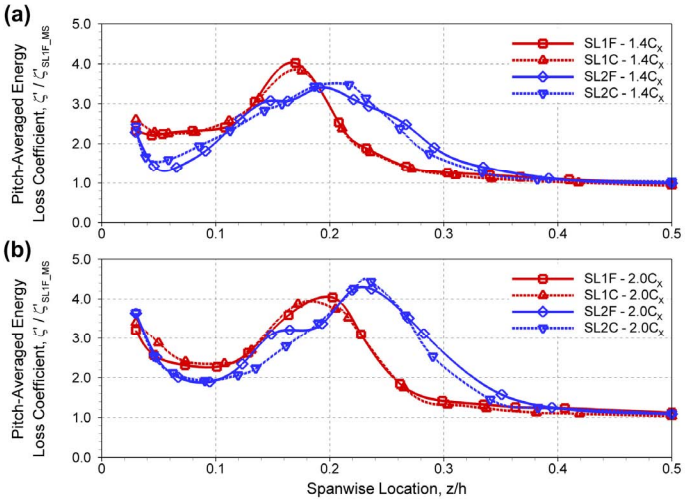

Figure 10. NORMALIZED PITCH-AVERAGED ENERGY LOSS COEFFICIENTS: (a) 1.4C_X AND (b) 2.0C_X

The overall-integrated results (0 to 50% span), both mass-averaged and mixed-out, are shown in Tables 4 and 5. The inlet boundary-layer losses have been subtracted from the traverse results, and therefore the comparisons are based on actual row losses. Further details about the treatment of the near-wall results (0 to 3% span) can be found in [29]. The constant-area mixing-out calculations were performed using continuity and momentum conservations, with free-slip walls, to reach complete equilibrium. The mixed-out results include additional losses due to primary and secondary kinetic energy dissipation, as well as changes in static pressure (e.g. pressure recovery [7]). This method, on the other hand, does not account for the additional loss production on the endwalls downstream of the measurement planes. Consequently in Tables 4 and 5, the mixed-out values from 2.0C_X are larger than those from 1.4C_X, consistent with the findings in [24,35]. The additional losses, however, do not affect the trends in the data. SL1F and SL1C produce similar mass-averaged row losses in both measurement planes despite small differences in C_{SKE}. The results at 2.0C_X display about a 30% reduction in C_{SKE} and a 20% increase in row losses. The mixed-out values are also very similar for the two cascades, although the additional mixing losses from 2.0C_X are smaller than those from 1.4C_X. This is attributed to the more uniform flow fields at 2.0C_X. Notwithstanding the small differences, it may be concluded that the collective effects of endwall contouring in SL1C, which may appear aggressive [15], have not adversely affected the aerodynamic performance.

Table 4. OVERALL INTEGRATED RESULTS FOR SL1F AND SL1C

SL1 Integrated Results: 0 to 50% Span	Secondary Kinetic Energy Coefficient, C''_{SKE}		Normalized Row Loss Coefficient, $\zeta''/\zeta''_{SL1F\_1.4Cx}$	
	SL1F	SL1C	SL1F	SL1C
1.4C_X	0.0014	0.0012	**1.00**	0.99
Mixed-Out from 1.4C_X	-	-	1.14	1.12
2.0C_X	0.0010	0.0008	1.20	1.19
Mixed-Out from 2.0C_X	-	-	1.29	1.28

In contrast to SL1, the SL2 results in Table 5 show larger SKE dissipation and higher mixing losses downstream of 1.4C_X. In particular, the mass-averaged row losses in SL2F have risen by 33% at 2.0C_X. SL2C, on the other hand, displays smaller changes between the two planes as anticipated from Figures 8a and 9a. Overall, the results at 2.0C_X indicate reductions in both mass-averaged (5%) and mixed-out (7%) row losses due to endwall contouring. In an engine environment, the additional benefit associated with reduced SKE and under/overturning would typically be realized in the downstream blade rows.

Table 5. OVERALL INTEGRATED RESULTS FOR SL2F AND SL2C

SL2 Integrated Results: 0 to 50% Span	Secondary Kinetic Energy Coefficient, C''_{SKE}		Normalized Row Loss Coefficient, $\zeta''/\zeta''_{SL2F\_1.4Cx}$	
	SL2F	SL2C	SL2F	SL2C
1.4C_X	0.0056	0.0035	**1.00**	1.00
Mixed-Out from 1.4C_X	-	-	1.26	1.19
2.0C_X	0.0042	0.0027	1.33	1.26
Mixed-Out from 2.0C_X	-	-	1.55	1.44

As a final note, comments have been made recently regarding the suitability of C_{SKE} as the objective function for design optimization [21,35,36]. In the present study, SKE dissipation between 1.4C_X and 2.0C_X accounts for less than 15% of the additional losses, as the majority of the mixing losses appear to arise from primary kinetic energy dissipation, including shearing losses at the endwalls, as well as pressure force effects. These results are in agreement with the findings in [32], suggesting larger primary kinetic energy dissipation rates in high-speed flows. Furthermore, the experimental results at 1.4C_X do not corroborate the CFD predictions regarding the mass-averaged row losses. The mixed-out losses, on the other hand, indicate improvements for the more highly-loaded cascade. In view of this, some of the future research objectives are to examine the role of turbulence modeling in capturing the mixing losses in transonic flows, and to assess the suitability of the mixed-out energy loss coefficient as the objective function for contouring design.

CONCLUSIONS

Results from an experimental investigation of the secondary flows in two transonic linear turbine cascades, with both flat and contoured endwalls, were presented here. The method of Praisner et al. [3], modified for compressible CFD calculations, was used to optimize the wall geometries, and thereby to redistribute the pressure gradients near the endwalls. Overall, the application of endwall contouring led to weaker interactions between the vortical structures and the suction-surface boundary layers, and more favourable (streamwise-oriented) mid-passage crossflows based on the surface flow visualization results, at the expense of increased wetted areas.

The initial measurements downstream of the cascades at 1.4C_X, however, did not confirm the numerically predicted loss reductions. The aerodynamic performance of the lower loaded cascades, SL1F and SL1C, showed negligible changes due to contouring. The more highly-loaded contoured cascade, SL2C, on the other hand, produced smaller and less intense vortical structures, and lower SKE than SL2F. This was accompanied by reduced under/overturning from 5% to 50% span, validating the

CFD predictions. The second set of measurements at $2.0C_X$ displayed lower mass-averaged row losses for the contoured cascades, associated with reduced mixing losses between the two planes. Consequently, the fully mixed-out results showed 7% loss reduction in SL2C as compared to SL2F. These results confirmed the low-speed findings in cascades with similar endwall designs [23,24], that contouring is a viable method to reduce the secondary losses.

Although the application of contouring has positively influenced the aerodynamic performance in both cases, secondary loss predictions in high-speed flows and, in particular, the contributions from SKE dissipation require further analysis. The discrepancies between the numerical predictions and the measurements also highlight the need for detailed experimental studies. Ongoing research is focused on the effects of turbulence modeling on the prediction of loss generation within the blade rows, and the effectiveness of endwall contouring at off-design Mach numbers.

ACKNOWLEDGMENTS

The financial and technical support of Pratt & Whitney Aircraft (PWA) is gratefully acknowledged. The first author also gratefully acknowledges the financial support of the Government of Ontario through Ontario Graduate Scholarships (OGS).

NOMENCLATURE

a	speed of sound
$AVDR$	axial velocity density ratio (Eqn. 1)
C	blade chord length
C_{SKE}	secondary kinetic energy coefficient (Eqn. 8)
$C\omega_S$	streamwise vorticity coefficient (Eqn. 6)
h	blade span, enthalpy
H	boundary layer shape factor
M	Mach number
PS	pressure surface/side
Re	Reynolds number
RVR	row velocity ratio
s	blade pitch, entropy
S	blade surface length
SS	suction surface/side
U,V	resultant flow velocity
u,v,w	axial, pitchwise and spanwise velocity
x,y,z	axial, pitchwise and spanwise distance
Y	total pressure loss coefficient
Zw	Zweifel coefficient (Eqn. 2)
α	spanwise flow angle
β	pitchwise flow angle (from axial)
γ	specific heat ratio
δ	boundary layer thickness
δ^*	boundary layer displacement thickness
ζ	energy loss coefficient (Eqn. 3)
θ	boundary layer momentum thickness
ρ	air density
ς	blade stagger angle
ω	vorticity

Subscripts

0	stagnation
1,2	cascade inlet and outlet
is	isentropic
MS	midspan
prim	primary
sec	secondary
X,Y,Z,S	axial, pitchwise, spanwise and streamwise

Superscripts

'	pitch-averaged
"	overall-averaged

REFERENCES

[1] Denton, J. D., 1993, "Loss Mechanisms in Turbomachines," ASME J. Turbomach., **115** (4), pp. 621-656.

[2] Taremi, F., Sjolander, S.A. and Praisner, T., 2010, "Measurements of Endwall Flows in Transonic Linear Turbine Cascades: Part II - High Flow Turning," Proc. ASME Turbo Expo 2010 (GT2010-22760), Glasgow, Scotland, UK.

[3] Praisner, T.J., Allen-Bradley, E., Grover, E.A., Knezevici, D.C. and Sjolander, S.A., 2007, "Application of Non-Axisymmetric Endwall Contouring to Conventional and High-Lift Turbine Airfoils," Proc. ASME Turbo Expo 2007 (GT2007-27579), Montreal, Canada.

[4] Sieverding, C. H., 1985, "Recent Progress in the Understanding of Basic Aspects of Secondary Flows in Turbine Blade Passages," ASME J. Turbomach., **107** (2), pp. 249–257.

[5] Langston, L. S., 2001, "Secondary Flows in Axial Turbines - A Review," Annals of the New York Academy of Sciences, **943**, pp. 11-26.

[6] Weiss, A.P. and Fottner, L., 1995, "The Influence of Load Distribution on Secondary Flow in Straight Turbine Cascades," ASME J. Turbomach., **117** (1), pp. 133-141.

[7] Benner, M.W., Sjolander, S.A. and Moustapha, S.H., 2004, "The Influence of Leading-Edge Geometry on Secondary Losses in a Turbine Cascade at the Design Incidence," ASME J. Turbomach., **126** (2), pp. 277-287.

[8] Zoric, T., Popovic, I., Sjolander, S.A., Praisner, T. and Grover, E., 2007, "Comparative Investigation of Three Highly Loaded LP Turbine Airfoils: Part I - Measured Profile and Secondary Losses at Design Incidence," Proc. ASME Turbo Expo 2007 (GT2007-27537), Montreal, Canada.

[9] Duden, A., Raab, I. and Fottner, L., 1999, "Controlling the Secondary Flow in a Turbine Cascade by Three-Dimensional Airfoil Design and Endwall Contouring," ASME J. Turbomach., **121** (2), pp. 191-199.

[10] Dossena, V., Perdichizzi, A. and Savini, M., 1999, "The Influence of Endwall Contouring on the Performance of a Turbine Nozzle Guide Vane," ASME J. Turbomach., **121** (2), pp. 200-208.

[11] Harvey, N.W., Rose, M.G., Taylor, M.D., Shahpar, S., Hartland, J. and Gregory-Smith, D.G., 2000, "Nonaxisymmetric Turbine End Wall Design: Part I - Three-Dimensional Linear Design System," ASME J. Turbomach., **122** (2), pp. 278-285.

[12] Hartland, J.C., Gregory-Smith, D.G., Harvey, N.W. and Rose, M.G., 2000, "Nonaxisymmetric Turbine End Wall Design: Part II - Experimental Validation," ASME J. Turbomach., **122** (2), pp. 286-293.

[13] Ingram, G., Gregory-Smith, D., Rose, M., Harvey, N. and Brennan, G., 2002, "The Effect of End-Wall Profiling on Secondary Flow and Loss Development in a Turbine Cascade," Proc. ASME Turbo Expo 2002 (GT2002-30339), Amsterdam, The Netherlands.

[14] Ingram, G., Gregory-Smith, D. and Harvey, N., 2005, "The Benefits of Turbine Endwall Profiling in a Cascade," Proc. Instn. Mech. Engrs., Part A: J. Power and Energy, **219** (A1), pp. 49-59.

[15] Ingram, G., Gregory-Smith, D. and Harvey, N., 2005, "Investigation of a Novel Secondary Flow Feature in a Turbine Cascade With End Wall Profiling," ASME J. Turbomach., **127** (1), pp. 209-214.

[16] Gregory-Smith, D., Bagshaw, D., Ingram, G. and Stokes, M., 2008, "Using Profiled Endwalls, Blade Lean and Leading Edge Extensions to Minimize Secondary Flow," Proc. ASME Turbo Expo 2008 (GT2008-50811), Berlin, Germany.

[17] Rose, M.G., Harvey, N.W., Seaman, P., Newman, D.A. and McManus, D., 2001, "Improving the Efficiency of the Trent 500 HP Turbine Using Nonaxisymmetric End Walls. Part II: Experimental Validation," Proc. ASME Turbo Expo 2001 (GT2001-0505), New Orleans, LA, USA.

[18] Harvey, N.W., Brennan, G., Newman, D.A. and Rose, M.G., 2002, "Improving Turbine Efficiency Using Non-Axisymmetric End Walls: Validation in the Multi-Row Environment and With Low Aspect Ratio Blading," Proc. ASME Turbo Expo 2002 (GT2002-30337), Amsterdam, The Netherlands.

[19] Gustafson, R., Mahmood, G. and Acharya, S., 2007, "Aerodynamic Measurements in a Linear Turbine Blade Passage With Three-Dimensional Endwall Contouring," Proc. ASME Turbo Expo 2007 (GT2007-28073), Montreal, Canada.

[20] Torre, D., Vázquez, R., de la Rosa Blanco, E. and Hodson, H.P., 2011, "A New Alternative for Reduction in Secondary Flows in Low Pressure Turbines," ASME J. Turbomach., **133** (1), p. 011029.

[21] Schuepbach, P., Rose, M., Gier, J., Raab, I., Germain, T. and Abhari, R., 2009, "Non-Axisymmetric End Wall Profiles Including Fillet Radii, in a 1.5 Stage Axial Flow Turbine," Proc. 8th European Conference on Turbomachinery Fluid Dynamics and Thermodynamics, Graz, Austria.

[22] Germain, T., Nagel, M., Raab, I., Schüpbach, P., Abhari, R.S. and Rose, M., 2010, "Improving Efficiency of a High Work Turbine Using Nonaxisymmetric Endwalls - Part I: Endwall Design and Performance," ASME J. Turbomach., **132** (2), p. 021007.

[23] Knezevici, D.C., Sjolander, S.A., Praisner, T.J., Allen-Bradley, E. and Grover, E.A., 2010, "Measurements of Secondary Losses in a Turbine Cascade With the Implementation of Nonaxisymmetric Endwall Contouring," ASME J. Turbomach., **132** (1), p. 011013.

[24] Knezevici, D.C., Sjolander, S.A., Praisner, T.J., Allen-Bradley, E. and Grover, E.A., 2009, "Measurements of Secondary Losses in a High-Lift Front-Loaded Turbine Cascade With the Implementation of Non-Axisymmetric Endwall Contouring," Proc. ASME Turbo Expo 2009 (GT2009-59677), Orlando, FL, USA.

[25] Brennan, G., Harvey, N.W., Rose, M.G., Fomilson, N. and Taylor, M.D., 2003, "Improving the Efficiency of the Trent 500-HP Turbine Using Nonaxisymmetric End Walls - Part I: Turbine Design," ASME J. Turbomach., **125** (3), pp. 497-504.

[26] Praisner, T.J. and Clark, J.P., 2007, "Predicting Transition in Turbomachinery - Part I: A Review and New Model Development," ASME J. Turbomach., **129** (1), pp. 1-13.

[27] Johansen, E.S., Rediniotis, O.K. and Jones, G., 2001, "The Compressible Calibration of Miniature Multi-Hole Probes," ASME J. Fluids Eng., **123** (1), pp. 128-138.

[28] Corriveau, D. and Sjolander, S.A., 2002, "Impact of Flow Quality in Transonic Cascade Wind Tunnels- Measurements in an HP Turbine Cascade," Proc. ICAS 2002 Congress, Toronto, Canada.

[29] Taremi, F., Sjolander, S.A. and Praisner, T., 2010, "Measurements of Endwall Flows in Transonic Linear Turbine Cascades: Part I - Low Flow Turning," Proc. ASME Turbo Expo 2010 (GT2010-22759), Glasgow, Scotland, UK.

[30] Jeffries, M.S., Jouini, D.B.M. and Sjolander, S.A., 1997, "Determining the Sampling Rates and Times in a High Speed Wind Tunnel," Proc. CASI 6th Symposium on Aerodynamics, Toronto, Canada.

[31] Brown, L. E., 1972, "Axial Flow Compressor and Turbine Loss Coefficients: A Comparison of Several Parameters," ASME J. Eng. Power, **94**, pp. 193-201.

[32] Perdichizzi, A., 1990, "Mach Number Effects on Secondary Flow Development Downstream of a Turbine Cascade," ASME J. Turbomach., **112** (4), pp. 643-651.

[33] MacIsaac, G.D., Taremi, F., Knezevici, D.C., Scribner, C.A. and Sjolander, S.A., 2009, "Challenges in Using Kiel and Seven-Hole Pressure Probes in Highly Three-Dimensional Flows: Application to Turbomachinery Cascade Measurements," Proc. 19th ISABE Conference (ISABE-2009-1209), Montreal, Canada.

[34] Moffat, R.J., 1982, "Contributions to the Theory of Single-Sample Uncertainty Analysis," ASME J. Fluids Eng., **104** (2), pp. 250-258.

[35] MacIsaac, G.D., Sjolander, S.A. and Praisner, T., 2010, "Measurements of Losses and Reynolds Stresses in the Secondary Flow Downstream of a Low-Speed Linear Turbine Cascade," Proc. ASME Turbo Expo 2010 (GT2010-22727), Glasgow, Scotland, UK.

[36] Snedden, G., Dunn, D., Von Backström, T.W. and Ingram, G., 2010, "Observations on the Selection of Objective Function for the Optimisation of Turbine Endwalls Using Computational Fluid Dynamics," Proc. 7th South African Conference on Computational and Applied Mechanics (SACAM10), Pretoria, South Africa.